

Mass classification of dark matter perturbers of stellar tidal streams

F. Montanari[★], and J. García-Bellido[†]

Instituto de Física Teórica IFT-UAM/CSIC, Universidad Autónoma de Madrid, Cantoblanco 28049 Madrid, Spain

22 December 2024

ABSTRACT

Stellar streams formed by tidal stripping of progenitors orbiting around the Milky Way are expected to be perturbed by encounters with dark matter subhalos. Recent studies have shown that they are an excellent proxy to infer properties of the perturbers, such as their mass. Here we present two different methodologies that make use of the fully non-Gaussian density distribution of stellar streams: a Bayesian model selection based on the probability density function (PDF) of stellar density, and a likelihood-free gradient boosting classifier. As an application, we forecast model selection strength of evidence for cold dark matter clusters of masses 10^3 – $10^5 M_\odot$, 10^5 – $10^7 M_\odot$ and 10^7 – $10^9 M_\odot$, based on a GD-1-like stellar stream and including realistic observational errors. Evidence for the smaller mass range, so far under-explored, is particularly interesting for the primordial black holes cold dark matter hypothesis. We expect moderate to strong evidence for model selection based on the PDF analysis when assuming low and intermediate dark matter perturbers mass ranges as fiducial models, but only weak evidence when the larger mass range is taken to be the fiducial model. Instead, the gradient boosting model is a highly efficient classifier (F_1 -scores larger than 90%) for all mass ranges here considered.

Key words: cosmology: dark matter – Galaxy: evolution – Galaxy: halo – Galaxy: kinematics and dynamics – Galaxy: structure

1 INTRODUCTION

The nature of dark matter (DM) remains one of the most elusive mysteries of modern cosmology. While the existence of dark matter can be inferred from multiple observations, from the CMB to dwarf galaxies, its mass and interactions, even its corpuscular-versus-wave nature, is still unknown. In the last few years a new contender, primordial black holes (PBH) dark matter, see e.g. [García-Bellido \(2017\)](#), has been reborn thanks to the LIGO detection of GW from massive BBH coalescence ([Abbott et al. 2016](#)). Their origin from the collapse of primordial fluctuations is rather generic ([García-Bellido et al. 1996](#)), but their mass range and clustering properties are mostly uncertain. Some scenarios predict large non-Gaussian tails in the matter density contrast distribution that could give rise to clusters of PBH ([Ezquiaga et al. 2020](#)), thus evading all of the observational constraints ([Clesse & García-Bellido 2018](#); [Carr et al. 2021](#)). The abundance, size and mass of these clusters is rather model dependent. What we can infer from N-body simulations is their density profile and their spatial distribution over the halos of galaxies ([Trashorras et al. 2020](#)). Their behaviour on large scales is indistinguishable from that of the usual collisionless dark matter components of cosmological N-body simulations that agree remarkably well with cosmological observations ([Zavala & Frenk 2019](#)). What differs from the usual particle dark matter (PDM) scenario is the small scale structure, and particularly the abundance and properties of subhalos with masses below $10^6 M_\odot$. Many of these PBH clusters evaporate via slingshot effects over the age of the universe, leaving dense cores

of $10^3 M_\odot$ ([Trashorras et al. 2020](#)). These small-mass PBH clusters orbit around the galaxy and interact with other collapsed objects like globular clusters and dwarf galaxies (see [Montanari et al. \(2019\)](#) for a prospective analysis constraining such interactions via trajectory intersections with Milky Way hyper-velocities stars). When these are tidally stretched by successive passages through the disk of the galaxy, they become what is known as tidal streams, almost one-dimensional concentrations of stars that stretch across the sky ([Allen & Richstone 1988](#); [Moore & Davis 1994](#); [Johnston et al. 1995](#)). These highly-extended stellar streams are excellent targets for dark compact clusters of stars or black holes orbiting the central halo of the galaxy ([Ibata et al. 2002](#); [Banik et al. 2019a](#); [Bonaca et al. 2019](#)). In this work we explore the possibility to distinguish and classify by mass the different perturbers that populate the galactic halo. In the future we may add to this analysis their size and concentration. Our ability to distinguish low-mass from high-mass clusters will then allow us to obtain information about the nature of dark matter. For instance, both Fuzzy DM and Warm DM predict that the smallest compact structures should have masses of order $10^7 M_\odot$, while axion miniclusters are typically in the range of $10^{-9} M_\odot$. While PDM is expected to cluster down to $10^{-6} M_\odot$ ([Bertschinger 2006](#)), we don't expect a peak abundance of DM clusters in the 10^3 – $10^5 M_\odot$ range. Therefore, a detection of density perturbations in stellar streams suggesting an excess of subhalos compared to PDM would be an indication of the PBH nature of DM. On the other hand, these intermediate mass scales are too small to be detected by strong gravitational lensing effects on the light of distant galaxies and too large to significantly affect the microlensing of nearby stars. Therefore, we propose these methods as a new way to explore the nature of DM.

A convolutional neural network was built by [Petac \(2019\)](#) to clas-

[★] E-mail: francesco.montanari@uam.es

[†] E-mail: juan.garciabellido@uam.es

sify DM subhalo masses based on Milky Way stars phase-space dynamics, expecting to be able to constrain masses down to $10^7 M_\odot$ in the near future. This lower limit is set in large part by the complicated stellar physics around the disk. In this work we focus on the Milky Way halo, and study stellar tidal stream dynamics in a regime where perturbation theory in the action-angle representation of streams applies (Bovy et al. 2017). The simplified picture allows us to reach high classification accuracy even for lower masses.

The density power spectrum of tidal streams was then studied by Bovy et al. (2017); Banik et al. (2018); Banik & Bovy (2019); Banik et al. (2019b); Banik et al. (2019a); Dalal et al. (2020), constraining the properties of perturbers for the Palomar 5 and GD-1 streams. Bovy et al. (2017) showed that not only the density, but also the mean track power spectrum and their bispectra contain important complementary information. The bispectrum is sensitive to profile asymmetries that are missed by the power spectrum. Given the non-Gaussian nature of density profiles, higher order correlation functions are likely to contain relevant information. Hermans et al. (2020) proposed a likelihood-free Bayesian inference pipeline built upon neural networks that avoids possibly insufficient summary statistic. In this work we also aim at profiting from the fully non-Gaussian information of stellar streams density profiles using machine learning techniques, but also a much simpler approach.

Bonaca et al. (2019, 2020) showed that the gaps and the spur observed in GD-1 are consistent with having originated from a collision with a single massive perturber, see also Gialluca et al. (2020). In this work we use a simulated GD-1-like tidal stream allowing the possibility of several impacts. Indeed, multiple impacts are expected in the standard cold dark matter (CDM) scenario, which for a GD-1-like stream amount to ~ 60 for perturbers in the range of masses 10^5 – $10^9 M_\odot$ (Erkal et al. 2016). This approach has the advantage of profiting from information coming not only from manifest features like large gaps, but from the full star distribution within the stream.

We present two novel methodologies aimed at constraining the mass of stellar streams dark matter perturbers. First, we outline a Bayesian model selection pipeline based on the PDF of stellar streams density perturbations. The PDF is a straightforward observable that takes into account the fully non-Gaussian information of density perturbations. Second, we consider a very different and complementary approach by training a gradient boosting classifier. As an application, we run simulations consistent with GD-1-like tidal stream and we forecast the possibility of selecting which one between different perturber mass ranges is favored by data. We consider a small 10^3 – $10^5 M_\odot$, intermediate 10^5 – $10^7 M_\odot$ and large 10^7 – $10^9 M_\odot$ range. The smallest mass range is so far unexplored and motivated by the fact that it is suitable to test the PBH CDM scenario which is more likely to form subhalo objects of such masses than vanilla CDM (García-Bellido 2017). This analysis will motivate future studies based on the specific statistical differences between PBH CDM and other DM models over the full 10^3 – $10^9 M_\odot$ mass range.

In section 2 we describe our simulated stellar streams. In section 3 we outline the two methodologies proposed to constrain DM clusters masses and show results in section 4. We conclude in section 5. Appendix A discusses convergence properties for our simulations. We release the scripts used throughout our analysis at <https://gitlab.com/montanari/stream-dm>.

2 SIMULATIONS

We model a smooth GD-1-like tidal stream relying on the line-of-parallel-angle approach developed in Bovy et al. (2017), based on

the action-angle representation of streams (Bovy 2014; Sanders et al. 2016). In this formalism statistical properties of cold streams are well described by the density ρ and mean track of parallel frequency $\langle \Omega_\parallel \rangle$ (average frequency along the stream) as a function the angle offset $\Delta\theta_\parallel$ (parallel to the direction along which the stream stretches) from the progenitor. The transformation from angle-frequency space in the neighbourhood of the stream to observable configuration space can be computed efficiently (Bovy 2014), allowing to assess the effect of observational errors.

Numerical simulations rely on `galpy`¹ (Bovy 2015) and its extension `streamgap-pepper`² (Bovy et al. 2017). Statistical sampling of multiple impacts follows section 2.3 of Bovy et al. (2017) to which we refer for more details and that here we only briefly review focusing on aspects relevant when considering PBH CDM perturbers rather than vanilla CDM. We neglect perturbations induced by baryonic structures as they are expected to be subdominant for a GD-1-like stream (Hermans et al. 2020). The following quantities are sampled sequentially:

- (i) Impact time t_i . We sample 64 values of time, corresponding to an interval of ~ 140 Myr (smaller than the radial period ~ 400 Myr of the stream) given the 9 Gyr age of the stream.³
- (ii) Angular offset $\Delta\theta_{i\parallel}$ from the progenitor of closest approach along the stream.
- (iii) Fly-by velocity \mathbf{w} of the perturber, assuming a Gaussian distribution of CDM subhalos with dispersion σ_h (Erkal et al. 2016)).
- (iv) Mass M and internal structure of the perturber. The internal profile is described by the scale parameter r_s of an Hernquist profile (see appendix A for more details and a comparison with a Plummer profile).⁴ The mass M probability distribution is taken to be $p(M) \propto r_s(M) dn_h/dM$, where we further assume a CDM subhalo spectrum $dn_h/dM \propto M^{-2}$ (Yoon et al. 2011) and a scale factor obeying the deterministic relation $r_s(M) \propto M^{0.5}$ (Diemand et al. 2008).
- (v) Impact parameter b , uniformly sampled along the diameter of a cylindrical volume with radius b_{\max} around the stream (Erkal et al. 2016). Setting the radius proportional to the scale parameter, $b_{\max} = X r_s$, takes effectively into account that decreasing the perturber mass also the volume of interaction decreases. We set $X = 5$ as a compromise between computational convenience and numerical convergence of results (see appendix A).
- (vi) Number of impacts since the beginning of stream disruption to today, sampled from a Poisson distribution given the expected number $N_i = \sqrt{\frac{\pi}{2}} r_{\text{avg}} \sigma_h t_d^2 \Delta\Omega^m b_{\max} n_h$, where r_{avg} is the average spherical radius of the stream, t_d is the time corresponding to the start of the stream disruption, $\Delta\Omega^m$ is the mean parallel frequency parameter of the smooth stream, and n_h is the number of CDM sub-halos in the given mass range, estimated by extrapolating results

¹ <https://github.com/jobovy/galpy>.

² <https://github.com/jobovy/streamgap-pepper>.

³ We set this age to compare our results to those of Bovy et al. (2017) (see section A). More recent results suggest a lower fiducial value of 3.4 Gyr (Webb & Bovy 2019). As the stream length is proportional to the star velocity dispersion times its age, a younger stream (with the same length as the older one) would imply a larger velocity dispersion. However, the age estimate is very uncertain, our reference value of 9 Gyr being an upper limit. The age should eventually be marginalized over to compare with observations (Banik et al. 2019a).

⁴ The internal profile in the PBH CDM scenario differs from Hernquist and Plummer profiles as it shows a spike towards the center (Trashorras et al. 2020). However, this deviation only concerns a narrow innermost region of the perturber and does not affect our results.

compatible with the Via Lactea II simulation in the 10^6 – 10^7 mass range (Yoon et al. 2011; Bovy et al. 2017). Given the reference impact parameter factor $X = 5$, this brings $n_h \sim 839$, $n_h \sim 57$ and $n_h \sim 5$ in the 10^3 – $10^5 M_\odot$, 10^5 – $10^7 M_\odot$ and 10^7 – $10^9 M_\odot$ mass ranges of our interest, respectively.

Note that the effect of the dark matter encounters are well modeled in the impulse approximation as instantaneous velocity kicks (Bovy et al. 2017), neglecting effects of the collision on the perturber properties. To summarize, we sample from the following probability distribution:

$$\begin{aligned}
 p(t_i, \Delta\theta_{i\parallel}, \mathbf{w}, M, r_s, b, N_i) &= p(t_i) p(\Delta\theta_{i\parallel}|t_i) p(\mathbf{w}|t_i, \Delta\theta_{i\parallel}) \\
 &\quad p(M, r_s|t_i, \Delta\theta_{i\parallel}, \mathbf{w}) \\
 &\quad p(b|t_i, \Delta\theta_{i\parallel}, \mathbf{w}, M, r_s) \\
 &\quad p(N_i|t_i, \Delta\theta_{i\parallel}, \mathbf{w}, M, r_s, b)
 \end{aligned} \tag{1}$$

For each sample we retrieve the density profile as a function of the parallel angle offset from the progenitor $\Delta\theta_{\parallel}$.

We compute at least 1000 samples of perturbed density profiles for each mass range 10^3 – $10^5 M_\odot$, 10^5 – $10^7 M_\odot$ and 10^7 – $10^9 M_\odot$, shown in Figure 1 normalized such that the smooth profile is $\bar{\rho}_0 = 1$ close to the progenitor (see e.g. Figure 1 of Bovy et al. (2017) for more details about the unperturbed stream as a function of observable Galactic longitude). The smooth density profile is roughly constant up to $\Delta\theta_{\parallel} \approx 0.6$ and then it decreases. As expected, smaller mass perturbbers lead to smaller deviations from the smooth profile $\bar{\rho}$. More precisely, perturbations associated to 10^3 – $10^5 M_\odot$ perturbbers are at the $\sim 10\%$ level (larger only towards the tail), while those induced by 10^5 – $10^9 M_\odot$ perturbbers are much larger, rescaling ρ up to a factor ~ 4 . The perturbations profile is peaked towards the progenitor location $\Delta\theta_{\parallel} \rightarrow 0$ for large mass perturbbers (typically leading to $\rho/\bar{\rho} > 1$), and strongly skewed towards $\rho/\bar{\rho} < 1$ further away from the progenitor. Instead, perturbations induced by smaller mass objects are not peaked towards $\Delta\theta_{\parallel} \rightarrow 0$ and they are distributed more symmetrically around $\bar{\rho}$ up to the decrease at $\Delta\theta_{\parallel} \approx 0.6$. This suggests that perturbbers induce a gravitational drag towards the center of the stream, but the large number of impacts corresponding to the lower mass ranges symmetrizes the distribution around the smooth stream. Gravitational drag towards the center of the stream also induces skewness towards small density values at the already low density tail $\Delta\theta_{\parallel} > 0.6$ for the small mass range. As shown later in our results, these very different perturbed profiles makes it possible to easily classify the three perturbbers mass ranges here considered.

Note that for the low mass range the $\Delta\theta_{\parallel}$ corresponding to the density break of the smooth stream could be constrained within model uncertainties. However, in our simulations we fix the length of the stream and set its velocity dispersion based on its age (see also footnote 3 and section A).

The Jacobian of the change of coordinates between the parallel angle $\Delta\Omega_{\parallel}$ and the Galactic longitude l (Bovy et al. 2017) allows us to transform simulated density profiles $\rho(\Delta\Omega_{\parallel})$ to functions $\rho(l)$ of the observable Galactic longitude l . Our target is the density contrast normalized to the smooth profile, $Q\rho(l) = \rho(l)/\bar{\rho}(l)$,⁵ binned in longitude.⁶ The number $n_l \sim 300$ of angular bins spanning over

⁵ Here we introduce the quotient operator $Qx = x_1/x_0$, analog to the usual difference operator $\Delta x = x_1 - x_0$ (Henrici 1964). Note that Bovy et al. (2017) defines instead $\delta = \rho/\bar{\rho}$, but we avoid confusion with the common $\delta = (\rho - \bar{\rho})/\bar{\rho}$ notation used in cosmology.

⁶ $Q\rho(l)$ can be measured from observations following, e.g., the methodology of Banik et al. (2019a) or Hermans et al. (2020).

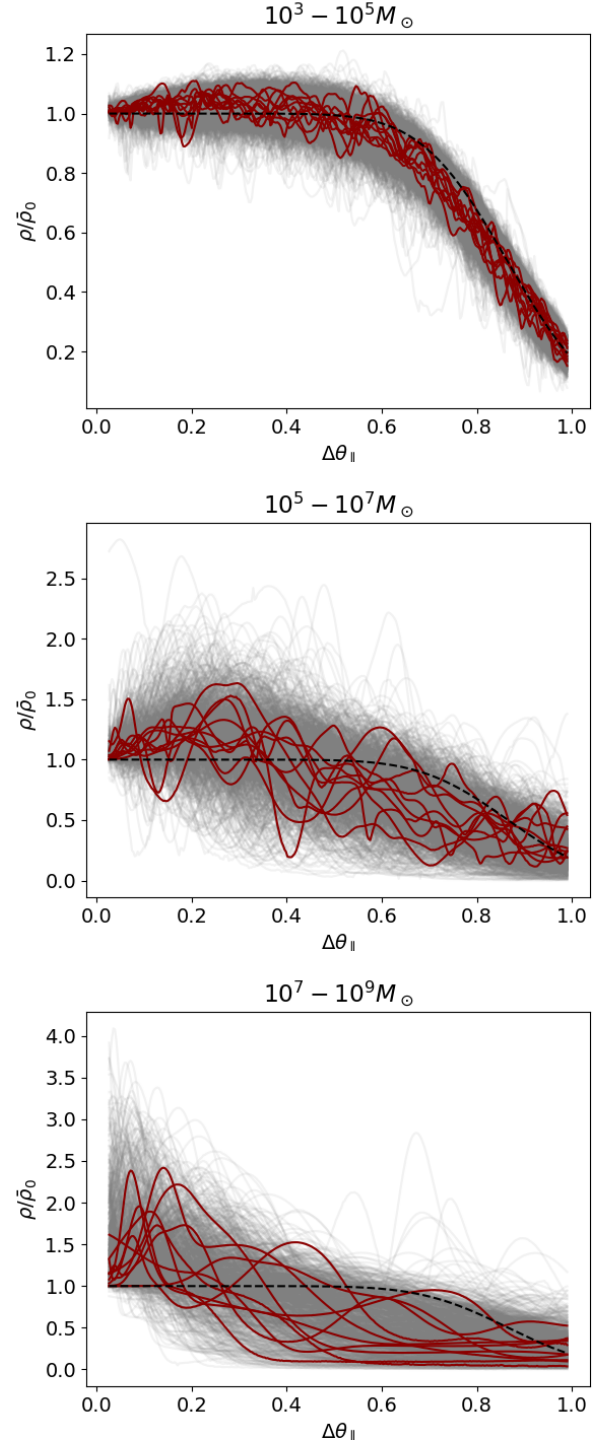


Figure 1. Simulated density profiles as a function of the parallel angle offset from the progenitor for different perturbbers mass ranges. Dashed lines are the smooth density profiles. Grey lines are the perturbed density profiles. Red lines are a random selection of the latter with the purpose of visually distinguish a few full profiles.

$\Delta l \approx 70^\circ$ gives a resolution of $\sim 0.2^\circ$. We assume Poisson shot noise $\epsilon(l) = 1/\sqrt{n(l)}$, where $n(l)$ is the star density per longitude. Following Bovy et al. (2017) we approximate shot noise to be 10% of the smooth density profile (see also Banik et al. (2018, 2019a) that show similar errors for angular bins along the stream), contributing to uncertainties in $Q\rho$ as $\sigma_\epsilon = 0.1$. Such an error is included by re-sampling density profiles from normal distributions with mean $\rho(l)$ and standard deviation σ_ϵ for each l .⁷ While the shot noise level is comparable to the size of perturbations for the lower mass range shown in Figure 1 (which does not include shot noise), it does not prevent us from discerning perturbations induced by large mass perturbors and hence to perform model selection. Note that such a level of shot noise alleviates errors due to extrapolation of N-body results down to the so far unexplored 10^3 – $10^5 M_\odot$ clusters range.

3 METHODS

In this section we outline two different methodologies for model selection: a simple Bayesian pipeline based on the PDF, and a gradient boosting classifier.

3.1 Bayesian model selection based on PDF

Here we outline a methodology to perform model selection based on Bayesian principles (Trotta 2017). Bovy et al. (2017) computed the power spectrum and the bispectrum of the density profile, showing that both probes contain valuable complementary information. Indeed, density perturbations are not expected to follow Gaussian profiles and even higher-order correlations than the bispectrum may contain valuable information. Therefore, rather than considering polyspectra, we compute the PDF of the density contrast profile $Q\rho(l)$.

3.1.1 Modeling the prior distribution

We compute histograms of simulated density profiles $Q\rho_i(l) = \rho_i(l)/\bar{\rho}_i(l)$ obtained sampling from Equation 1. Given the counts c_α for the α^{th} histogram bin of width w_α , the respective density is obtained as $y_\alpha = \frac{c_\alpha}{w_\alpha \sum_\beta c_\beta}$, where the normalization is such that the integral of the distribution is equal to one.⁸ This determines the probability density function $\text{PDF}(Q\rho)$. Figure 2 shows median values and interquartile ranges obtained computing the $\text{PDF}(Q\rho)$ for all simulations and for different choices of the number of bins N_{bin} . The range in $Q\rho$ is set to be the largest one where we have samples for both mass ranges. The $\text{PDF}(Q\rho)$ functions are peaked around $Q\rho \approx 1$, but consistently with Figure 1 the larger mass ranges have broader profiles. The $\text{PDF}(Q\rho)$ for the lower mass range is close to a normal distribution with mean $Q\rho = 1$ and standard deviation $\sigma = \sigma_\epsilon = 0.1$, consistently with the fact that it is dominated by shot noise ϵ . Neglecting shot noise would enhance negative skewness.

The PDF of each $\text{PDF}(Q\rho)$ bin y_α —i.e., $\text{PDF}(y_\alpha)$ —provides an estimate of the probability distribution $\Pi(y_\alpha|\mathcal{M})$ for model \mathcal{M} . Our models $\mathcal{M}_0, \mathcal{M}_1, \mathcal{M}_2$ correspond to the 10^3 – $10^5 M_\odot$, 10^5 – $10^7 M_\odot$ and 10^7 – $10^9 M_\odot$ mass ranges, respectively. The $\Pi(y_\alpha|\mathcal{M})$

⁷ Note that sampled values can be negative $\rho(l) < 0$, although the expectation value for the density must be positive by definition.

⁸ To avoid confusion with longitude bins l_j and with references to a given i^{th} sample of our simulations, we denote PDF histogram bins with Greek indices in the range $\alpha = 1, \dots, N_{\text{bin}}$.

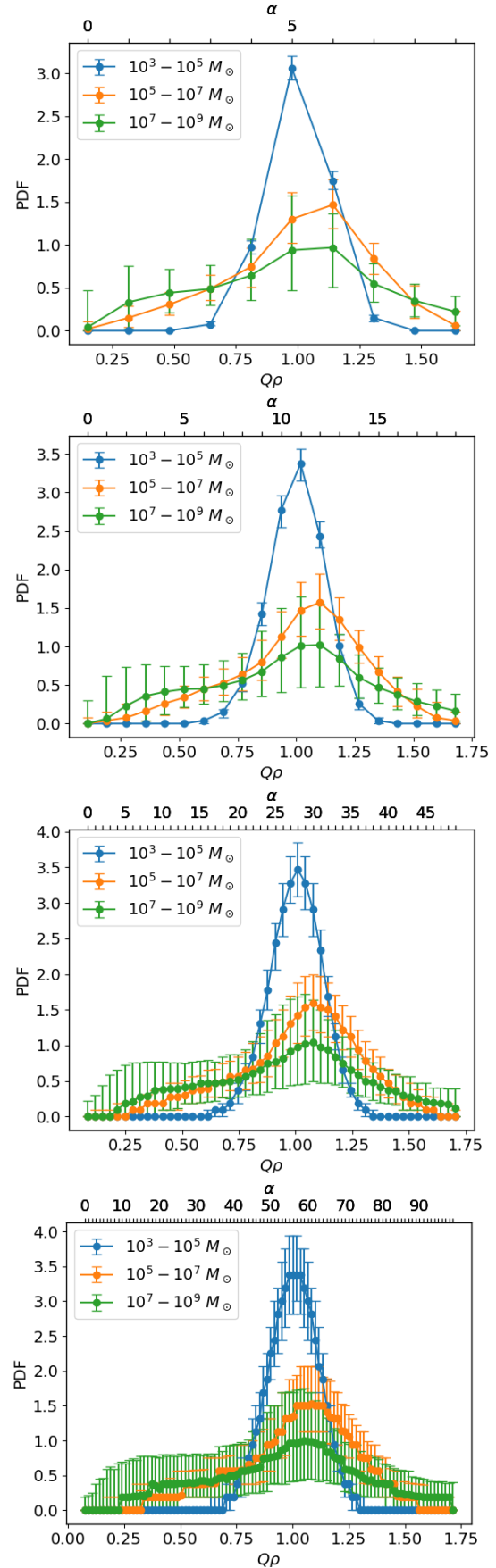


Figure 2. Interquartile ranges and medians for PDF bins of $Q\rho = \rho/\bar{\rho}$ profiles measured from simulations. Panels correspond, top to bottom, to $N_{\text{bin}} = 10, 20, 50, 100$, respectively. Top axes show the bin number.

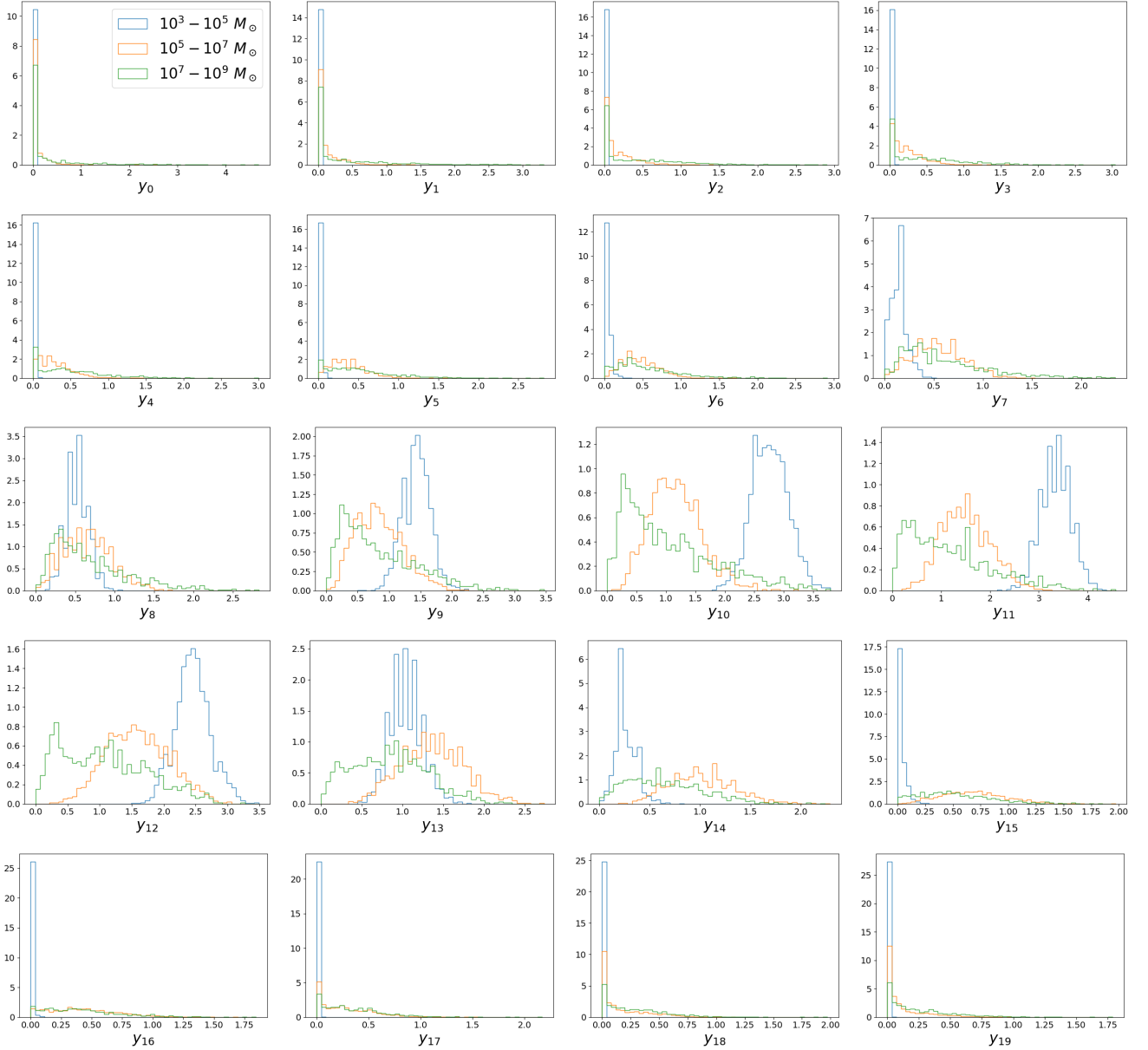


Figure 3. Panels show y_α distributions, namely the PDFs of each $\text{PDF}(Q\rho)$ bin α for the $N_{\text{bin}} = 20$ case (see Figure 2 for comparison). Here we recover each y_α using 50 bins, but when performing model selection we marginalize over 10–500 bins. In panels corresponding to the tails of $\text{PDF}(Q\rho)$ (i.e., small and large α values) we do not have enough resolution to estimate the PDF of the small mass case.

distributions so recovered based on simulations serves as prior for model selection. Figure 3 shows $\text{PDF}(y_\alpha)$ for all models. The small mass perturbers model is characterized by tiny y_α values for α bins corresponding to the tails of $\text{PDF}(Q\rho)$ (see Figure 2), while all mass models show a log-normal distribution for α bins corresponding central regions of $\text{PDF}(Q\rho)$.

3.1.2 Model selection

Let $p(\hat{y}_\alpha|y_\alpha, \mathcal{M})$ be the likelihood function for $\text{PDF}(Q\rho)$ bin α , where the hat denotes data. The Bayesian evidence for a given model \mathcal{M} is given by:

$$E(\hat{y}_\alpha|\mathcal{M}) = \int p(\hat{y}_\alpha|y_\alpha, \mathcal{M})\Pi(y_\alpha|\mathcal{M})dy_\alpha, \quad (2)$$

where the prior $\Pi(y_\alpha|\mathcal{M})$ is computed based on simulations as outlined above. Then, model selection can rely on the Bayes factor:

$$B_{\alpha,ij} = \frac{E(\hat{y}_\alpha|\mathcal{M}_i)}{E(\hat{y}_\alpha|\mathcal{M}_j)}. \quad (3)$$

Since an analysis based on true data is beyond the scope of this work, here we rely again on simulations to estimate $p(\hat{y}_\alpha|y_\alpha, \mathcal{M})$ in Equation 2 to forecast expected evidence values that will motivate further investigation based on true data. We consider different fiducial models:

$$p(\hat{y}_\alpha^{\text{fid},i}|y_\alpha) = \Pi(y_\alpha|\mathcal{M}_i), \quad (4)$$

for $i = 0, 1, 2$. Note that we removed the dependence on the model on the left-hand side, as for each fiducial case i we assume the likelihood to be the same; it is easy to relax this assumption if needed. Then we

consider

$$E(\hat{y}_{\alpha}^{\text{fid},i} | \mathcal{M}_j) = \int_0^{\infty} p(\hat{y}_{\alpha}^{\text{fid},i} | y_{\alpha}) \Pi(y_{\alpha} | \mathcal{M}_j) dy_{\alpha}, \quad (5)$$

where again $j = 0, 1, 2$. This determines

$$B_{\alpha,i,j}^{\text{fid},i} = E(\hat{y}_{\alpha}^{\text{fid},i} | \mathcal{M}_i) / E(\hat{y}_{\alpha}^{\text{fid},i} | \mathcal{M}_j), \quad (6)$$

which provides the strength of evidence for model \mathcal{M}_i if the true underlying mass distribution is indeed consistent with \mathcal{M}_i .

We sample $\Pi(y_{\alpha} | \mathcal{M}_i)$ using the same binning in y_{α} for all models \mathcal{M}_i so that the product of the two distributions can be estimated by the product of the respective bin heights, and integrals are estimated using the trapezoidal rule. Methodological errors are estimated by marginalizing over the number of bins in y_{α} .

3.2 Gradient Boosting classifier

We use the Python libraries `Scikit-learn` (Pedregosa et al. 2011) and `XGBoost` (Chen & Guestrin 2016) to train a gradient-boosted decision trees classifier. This model builds an ensemble of weak predictors (decision trees) to provide a robust predictor, optimizing an objective function with an iterative gradient descent algorithm. In our multi-class classification case the objective is a softmax function, whose output are the probabilities of each class being associated with a given input sample (Goodfellow et al. 2016). As we perform single-label classification (exclusive classes), the probabilities from all classes sum to one.

Our data is composed by a vector \mathbf{X} whose component i is a given simulation sample $(Q\rho_i(l_1), Q\rho_i(l_2), \dots, Q\rho_i(l_{n_l}))$, where $Q\rho_i(l) = \rho_i(l) / \bar{\rho}_i(l)$, and a vector \mathbf{y} containing binary labels associated to the class corresponding to a given sample. We randomly split the density samples into testing (25% of the total samples), training and validation (75% and 25% of the remaining samples, respectively) sets. The training and validation samples are used to tune the model hyperparameters, while the testing sample is only used to evaluate the accuracy of the final model. Then, rather than considering all of the n_l angular bins for each sample, we find it convenient to perform a Principal Component Analysis (PCA), and only keep $n_{\text{PCA}} < n_l$ components. PCA is sensitive to the variance of the features X_i that varies significantly in size. Hence, before computing the principal components we standardize the features by removing the mean and scaling to unit variance.

We then perform a 5-fold cross validation (CV) on the training set to optimize the maximum tree depth `max_depth` for base learners and the number of gradient boosted trees `n_estimators`. We find that optimizing the boosting learning rate does not affect substantially our results, due to its strong correlation with `n_estimators`. The search grid covers a few values for each hyperparameter (the full model has to be evaluated at each CV fold) within the `max_depth` $\in [2, 128]$ and `n_estimators` $\in [10, 200]$ ranges. The validation set is then used to evaluate the model pipeline based on the number of true positives T_{p_i} , true negatives T_{n_i} , false positives F_{p_i} and false negatives F_{n_i} for each class \mathcal{M}_i . As summary metrics we consider the precision

$$P_i = \frac{T_{p_i}}{T_{p_i} + F_{p_i}}, \quad (7)$$

recall

$$R_i = \frac{T_{p_i}}{T_{p_i} + F_{n_i}}, \quad (8)$$

and their harmonic average, or F_1 -score

$$F_{1,i} = \frac{2}{1/P_i + 1/R_i}. \quad (9)$$

We do not consider accuracy

$$A_i = \frac{T_{p_i} + T_{n_i}}{T_{p_i} + T_{n_i} + F_{p_i} + F_{n_i}},$$

as it would reflect the class imbalance that we have in our simulated dataset and, as such, it is not informative about classification performance.

We find that setting $n_{\text{PCA}} = 64$ explains 90% of the total variance and it is a reasonable compromise between good model performance and training speed. Setting a much lower or larger n_{PCA} (or not performing PCA) would worsen model performance by a few percentage points. While we expect that including more PCA components (or not performing PCA) should lead to at least comparable performance, this would require to run the CV search on a finer grid of hyperparameters. Furthermore, including more PCA components is up to 5 times more requiring in training speed.

4 RESULTS

In this section we discuss results for both mass model selection methodologies outlined above.

4.1 Bayesian model selection based on PDF

Figure 4 shows evidence ratios defined in Equation 6 for different choices of the number N_{bin} of bins in $Q\rho$. For each PDF($Q\rho$) bin y_{α} we compute the evidence ratio selecting different number of bins 10–500. Error bars correspond to interquartile ranges so obtained and their narrowness confirms that our evidence estimates based on the trapezoidal rule are robust against the binning in y_{α} .

Results shown in Figure 4 are easily interpreted comparing with Figure 2 and Figure 3. Central α bins show the largest Bayes factor, as PDF($Q\rho$) for the different models are significantly distinct. The crossing of PDF($Q\rho$) curves in Figure 2 (see also $\alpha = 8, 13$ in Figure 3) leads to a decrease in $\log B$ as the models are less distinguishable, while it increases again towards the tails where the small mass model \mathcal{M}_0 has PDF($Q\rho$) ≈ 0 . $\log B$ eventually decreases for the outer bins as PDF($Q\rho$) $\rightarrow 0$ also for the larger mass models \mathcal{M}_1 , \mathcal{M}_2 . Bins corresponding to the tails of PDF($Q\rho$) distributions do not give reliable evidence estimates due to the poor resolution for small mass perturbations which leads to a single PDF(y_{α}) bin, see Figure 3. Hereon we neglect evidence for α bins outside the $3\sigma_{\epsilon}$ range from the peak of the low mass PDF($Q\rho$) distribution, which is the most affected one by poor resolution.⁹ The excluded regions are shown as gray bands in Figure 4.

The largest Bayes factors are in the range 2.5–6, depending on N_{bin} , when the fiducial model is \mathcal{M}_0 (see $\log B_{01}^{\text{fid},0}$). Bayes factors are smaller when the fiducial models are \mathcal{M}_1 or \mathcal{M}_2 , as the corresponding PDF($Q\rho$) profiles (see Figure 2 and Figure 3) are less sharp and characterized by larger dispersion. While a proper estimate of cumulative Bayes factors should include their covariance, an upper limit is given by summing $\log B_{\alpha}$ for all α indices (up to the excluded region commented above) as reported in Table 1. Assuming models

⁹ See subsection 3.1.1 for a discussion about how σ_{ϵ} affects the lower mass PDF, which justifies our choice here.

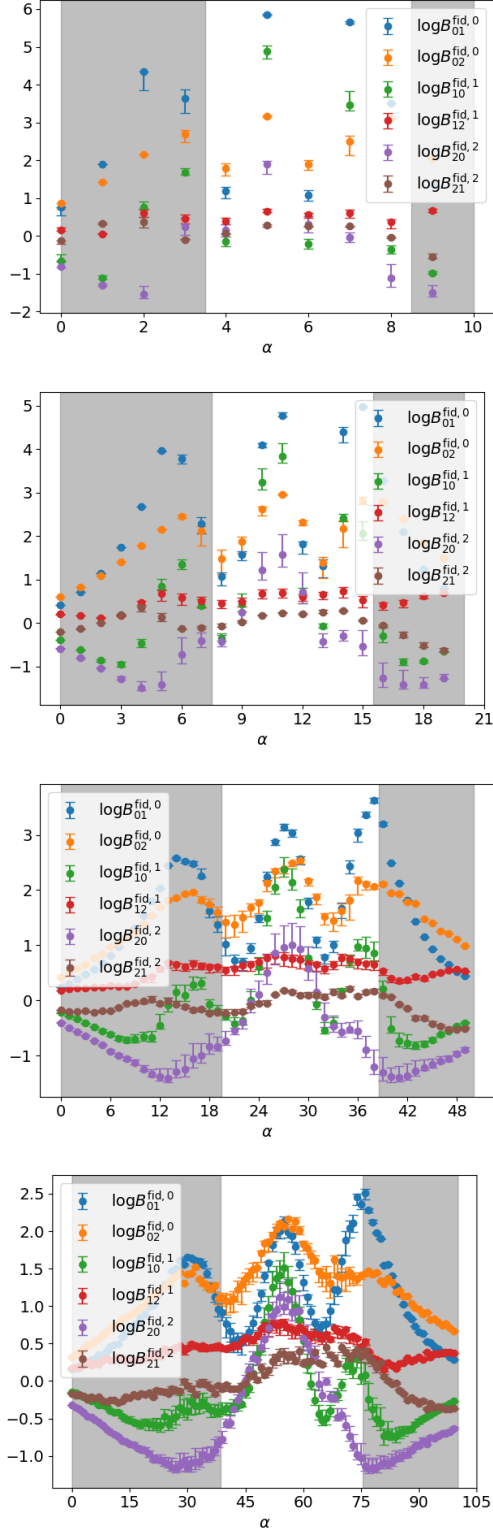


Figure 4. Bayes factors for different bins α of the PDF (see Figure 2) corresponding, top to bottom, to $N_{\text{bin}} = 10, 20, 50, 100$, respectively. Grey regions correspond to rare density fluctuations (not well sampled by our simulations) leading to unreliable evidence estimates.

Table 1. Cumulative Bayes factors for different choices of the number of PDF($Q\rho$) bins.

N_{bin}	10	20	50	100
$\sum \log B_{01}^{\text{fid},0}$	13.8	19.0	33.9	46.1
$\sum \log B_{02}^{\text{fid},0}$	9.3	14.8	34.4	57.0
$\sum \log B_{10}^{\text{fid},1}$	8.0	10.1	11.8	9.2
$\sum \log B_{12}^{\text{fid},1}$	2.2	4.3	12.4	22.4
$\sum \log B_{20}^{\text{fid},2}$	2.3	2.6	0.1	4.7
$\sum \log B_{21}^{\text{fid},2}$	0.9	1.1	0.6	7.5

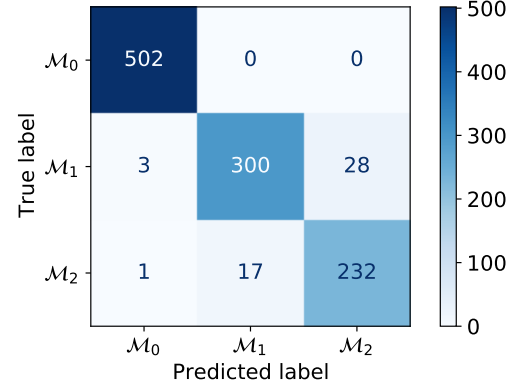


Figure 5. Confusion matrix obtained evaluating the gradient boosting model on the test dataset. Elements show the number of samples predicted to be associated to models \mathcal{M}_0 (10^3 – $10^5 M_\odot$ CDM perturbbers), \mathcal{M}_1 (10^5 – $10^7 M_\odot$) and \mathcal{M}_2 (10^7 – $10^9 M_\odot$) that are correctly (diagonal) or wrongly (non-diagonal) classified.

Table 2. Performance, relative to each mass category, of the gradient boosting classifier evaluated on the test set.

	Precision	Recall	F_1 -score	Support
10^3 – $10^5 M_\odot$	0.99	1.00	1.00	502
10^5 – $10^7 M_\odot$	0.95	0.91	0.93	331
10^7 – $10^9 M_\odot$	0.89	0.93	0.91	250

\mathcal{M}_0 or \mathcal{M}_1 as fiducial leads to moderate or strong evidence.¹⁰ Assuming model \mathcal{M}_2 can instead lead to inconclusive evidence. The largest evidences obtained when including more bins are expected to be more strongly suppressed by a proper covariance computation as they will be more correlated.

The analysis suggests that if CDM perturbbers form clusters in the 10^7 – $10^9 M_\odot$ range it may be more difficult to exclude the 10^3 – $10^5 M_\odot$ or 10^5 – $10^7 M_\odot$ hypotheses than the vice versa, possibly leading to inconclusive results.

4.2 Gradient Boosting classifier

Here we use the test set described in subsection 3.2 to evaluate the performance of the model trained on the training and validation sets. Given a X_i sample from the test set, the model outputs the probabilities of it being associated with the \mathcal{M}_0 , \mathcal{M}_1 and \mathcal{M}_2 classes,

¹⁰ We recall that the usual Jeffreys’ scale interprets $|\log B|$ ranges < 1 , 1–2.5, 2.5–5 and > 5 as inconclusive, weak, moderate and strong evidence, respectively Trotta (2017). See, however, Nesseris & García-Bellido (2013a).

respectively. To compute the number of (in-)correctly classified elements we select a given predicted class as the one with top-probability (we recall that the output probabilities from all the classes sum to 1) and compare with the true labels from the test set.

Figure 5 shows the confusion matrix reporting the number of correct classifications on the diagonal, and the number of wrong classifications on non-diagonal elements. Non-diagonal elements are much smaller than the diagonal ones, the largest confusion being among intermediate and large classes \mathcal{M}_1 , \mathcal{M}_2 . This is consistent with the PDF analysis, although the gradient boosting algorithm still shows strong discriminating power even for the large masses. This is confirmed by Table 2 showing the metrics described in Equation 7–Equation 9 evaluated on the test set. All classes are characterized by $\gtrsim 90\%$ scores, reaching even $\gtrsim 99\%$ scores for small masses \mathcal{M}_0 .

Finally, we note variations up to a couple of percentage points in summary metrics depending on random seeds used in the analysis pipeline, suggesting that it would further benefit from a larger training data set.

5 CONCLUSIONS

In our search for understanding one of the most elusive mysteries of nature, we have explored the information content associated with tidal stream collisions with dark matter clusters in the inner halo of our galaxy. We have introduced two complementary methodologies to constrain the mass of CDM perturbations on stellar streams and forecasted their potential ability based on GD-1-like stream simulations.

The Bayesian PDF model selection provides a straightforward and robust analysis that, contrary to incomplete statistics such as the power spectrum, takes into account the fully non-Gaussian information of stellar streams density profiles. Including realistic observational errors, we expect large Bayes factors when taking the low (10^3 – $10^5 M_\odot$, where a peak abundance of PBH CDM is expected) and intermediate (10^5 – $10^7 M_\odot$) mass perturbations as the fiducial models. Instead, taking a large masses (10^7 – $10^9 M_\odot$) model as the fiducial one may lead to inconclusive evidence, due to a larger dispersion in the PDF.

On the other hand, the gradient boosting model provides a complementary method to the PDF that allows to classify an observed density profile according to the most likely mass range with high performance. While the PDF analysis relies on Bayesian model selection, this is not the case for the gradient boosting one; however, the path integral approach developed in Nesseris & García-Bellido (2013b) to compute Bayesian credible intervals for non-parametric genetic algorithms can also be adapted to our gradient boosting model. The excellent performance of the gradient boosting classifier also relies on the fact that the model takes into account the ordered information about the density profile dependence on the longitude, information that is instead lost in the PDF analysis. Figure 1 shows indeed an important dependence of perturbations on the angular distance from the progenitor, including a characteristic profile peaked towards the progenitor for large mass perturbations (10^7 – $10^9 M_\odot$, which may bring to inconclusive evidence based on the PDF), differently from the low and intermediate mass cases. Another advantage of the gradient boosting algorithm is that it is a likelihood-free approach, contrary to the PDF analysis. While in this work we assumed different fiducial models for the latter, applying the PDF method to observations will require a detailed modeling of the likelihood.

As an extension to the analysis presented here, we compared our gradient boosting classifier with a densely connected feedforward neural network classifier (Goodfellow et al. 2016), which gives com-

parable results only when neglecting shot-noise and being significantly less performing for realistic observational errors. We also do not expect convolutional neural networks to bring substantial improvements because, due to their translational invariance, they would lose information about density perturbations as ordered sequences depending on longitude. Recurrent neural networks may be an interesting perspective that do not suffer from such a limitation, but due to typically high computational costs and the already good performance of our gradient boosting predictor, we don't deem it as an urgent investigation. Another advantage of gradient boosting is that its hyperparameters are easily optimized, avoiding empirical iterations over different neural networks architectures.

We showed that stellar streams are a promising tool to investigate 10^3 – $10^5 M_\odot$ DM perturbations, a range outside the reach of other observations such as lensing and of interest to discriminate the PBH CDM hypothesis. In our motivation of comparing this small subhalo objects mass range with the large ones 10^5 – $10^9 M_\odot$ to favor PBH CDM over particle DM relies on the simplified assumption that each model only contributes subhalo objects in the respective mass ranges. However, subhalo abundance is a continuous function spanning all the scales 10^3 – $10^9 M_\odot$ in the PDM scenario (Bertschinger 2006). An important extension of our simplified picture is then to compare the PBH CDM against standard particle DM scenarios in the full 10^3 – $10^9 M_\odot$ range taking into account the respective perturbations abundance distributions. This will require N-body simulations down to $10^3 M_\odot$ scales for both DM models, not available to date (but see advances, e.g., from Trashorras et al. (2020)). Note that by extrapolating particle DM results down to the unexplored 10^3 – $10^5 M_\odot$ mass range as done here underestimates the abundance of PBH CDM clusters, and a proper computation may increase the discriminating potential as a higher abundance of PBH objects over shot noise would sharpen the PDF distribution. Joint classification of other properties of the perturbations besides their mass, such as their size and concentration, is also valuable additional information to discriminate different DM models (Bonaca et al. 2019). Besides density fluctuations investigated here, another relevant stream property in the line-of-parallel-angle approach is the track fluctuation (Bovy et al. 2017).

Our methodologies can be readily applied to the GD-1 stream for which density perturbations data are already available (Banik et al. 2019a; Hermans et al. 2020), complementing previous studies. It can also be extended to other streams, as long as the density profile along the stream is a good descriptor of the stellar dynamics, which is certainly the case for other relatively cold streams such as Palomar 5 (Bovy et al. 2017). Depending on the stream, perturbations induced by baryonic objects, subleading for our GD-1-like case, may be relevant and needed to be modeled accurately as they may induce similar effects as DM subhalo objects of large mass. Current observations from the GAIA and Dark Energy Survey (DES) missions are increasingly improving data about known streams and discovering new streams (Li et al. 2019; Ibata et al. 2020), that will be further complemented with upcoming observations such as DESI (DESI Collaboration et al. 2016) and the Rubin Observatory (Ivezić et al. 2019), which provide new promising ground for dark matter constraints.

ACKNOWLEDGEMENTS

We thank Alex Drlica-Wagner and Ethan O. Naddler for useful discussion. We acknowledge use of the Hydra cluster at IFT-UAM/CSIC (Madrid). This work is supported by the Research Project PGC2018-

094773-B-C32 [MINECO-FEDER] and the Centro de Excelencia Severo Ochoa Program SEV-2016-0597.

REFERENCES

- Abbott B. P., et al., 2016, *Phys. Rev. Lett.*, 116, 241103 (arXiv:1606.04855)
- Allen A. J., Richstone D. O., 1988, *ApJ*, 325, 583
- Banik N., Bovy J., 2019, *Mon. Not. Roy. Astron. Soc.*, 484, 2009 (arXiv:1809.09640)
- Banik N., Bertone G., Bovy J., Bozorgnia N., 2018, *JCAP*, 1807, 061 (arXiv:1804.04384)
- Banik N., Bovy J., Bertone G., Erkal D., de Boer T., 2019a (arXiv:1911.02662)
- Banik N., Bovy J., Bertone G., Erkal D., de Boer T. J. L., 2019b, arXiv e-prints, p. arXiv:1911.02663 (arXiv:1911.02663)
- Bertschinger E., 2006, *Phys. Rev. D*, 74, 063509 (arXiv:astro-ph/0607319)
- Bonaca A., Hogg D. W., Price-Whelan A. M., Conroy C., 2019, *ApJ*, 880, 38 (arXiv:1811.03631)
- Bonaca A., et al., 2020, *ApJ*, 892, L37 (arXiv:2001.07215)
- Bovy J., 2014, *Astrophys. J.*, 795, 95 (arXiv:1401.2985)
- Bovy J., 2015, *Astrophys. J. Suppl.*, 216, 29 (arXiv:1412.3451)
- Bovy J., Erkal D., Sanders J. L., 2017, *Mon. Not. Roy. Astron. Soc.*, 466, 628 (arXiv:1606.03470)
- Carr B., Clesse S., García-Bellido J., Kuhnel F., 2021, *Phys. Dark Univ.*, 31, 100755 (arXiv:1906.08217)
- Chen T., Guestrin C., 2016, in Proceedings of the 22nd ACM SIGKDD International Conference on Knowledge Discovery and Data Mining. KDD '16. ACM, New York, NY, USA, pp 785–794, doi:10.1145/2939672.2939785, http://doi.acm.org/10.1145/2939672.2939785
- Clesse S., García-Bellido J., 2018, *Phys. Dark Univ.*, 22, 137 (arXiv:1711.10458)
- DESI Collaboration et al., 2016, arXiv e-prints, p. arXiv:1611.00036 (arXiv:1611.00036)
- Dalal N., Bovy J., Hui L., Li X., 2020 (arXiv:2011.13141)
- Diemand J., Kuhlen M., Madau P., Zemp M., Moore B., Potter D., Stadel J., 2008, *Nature*, 454, 735 (arXiv:0805.1244)
- Erkal D., Belokurov V., Bovy J., Sanders J. L., 2016, *MNRAS*, 463, 102 (arXiv:1606.04946)
- Ezquiaga J. M., García-Bellido J., Vennin V., 2020, *JCAP*, 2003, 029 (arXiv:1912.05399)
- García-Bellido J., 2017, *J. Phys. Conf. Ser.*, 840, 012032 (arXiv:1702.08275)
- García-Bellido J., Linde A. D., Wands D., 1996, *Phys. Rev.*, D54, 6040 (arXiv:astro-ph/9605094)
- Gialluca M. T., Naidu R. P., Bonaca A., 2020 (arXiv:2011.12963)
- Goodfellow I., Bengio Y., Courville A., 2016, *Deep Learning*. The MIT Press
- Henrici P., 1964, *Elements of numerical analysis*. Wiley, New York
- Hermans J., Banik N., Weniger C., Bertone G., Louppe G., 2020 (arXiv:2011.14923)
- Ibata R. A., Lewis G. F., Irwin M. J., 2002, *Mon. Not. Roy. Astron. Soc.*, 332, 915 (arXiv:astro-ph/0110690)
- Ibata R., et al., 2020, arXiv e-prints, p. arXiv:2012.05245 (arXiv:2012.05245)
- Ivezić v., et al., 2019, *Astrophys. J.*, 873, 111 (arXiv:0805.2366)
- Johnston K. V., Spergel D. N., Hernquist L., 1995, *ApJ*, 451, 598 (arXiv:astro-ph/9502005)
- Li T. S., et al., 2019, *MNRAS*, 490, 3508 (arXiv:1907.09481)
- Montanari F., Barrado D., García-Bellido J., 2019, *Mon. Not. Roy. Astron. Soc.*, 490, 5647 (arXiv:1907.09298)
- Moore B., Davis M., 1994, *MNRAS*, 270, 209 (arXiv:astro-ph/9401008)
- Nessers S., García-Bellido J., 2013a, *JCAP*, 08, 036 (arXiv:1210.7652)
- Nessers S., García-Bellido J., 2013b, *Phys. Rev. D*, 88, 063521 (arXiv:1306.4885)
- Pedregosa F., et al., 2011, *Journal of Machine Learning Research*, 12, 2825
- Petac M., 2019, arXiv e-prints, p. arXiv:1910.02492 (arXiv:1910.02492)
- Sanders J. L., Bovy J., Erkal D., 2016, *MNRAS*, 457, 3817 (arXiv:1510.03426)
- Trashorras M., García-Bellido J., Nesseris S., 2020 (arXiv:2006.15018)
- Trotta R., 2017, (arXiv:1701.01467)
- Webb J. J., Bovy J., 2019, *MNRAS*, 485, 5929 (arXiv:1811.07022)
- Yoon J. H., Johnston K. V., Hogg D. W., 2011, *ApJ*, 731, 58 (arXiv:1012.2884)
- Zavala J., Frenk C. S., 2019, *Galaxies*, 7, 81 (arXiv:1907.11775)

APPENDIX A: CONVERGENCE TESTS FOR SMALL MASS PERTURBERS

In this section we repeat convergence tests explored in Bovy et al. (2017) to verify the reliability of numerical simulations for small masses perturbors 10^3 – $10^5 M_\odot$, and we study the effect of different perturber internal profiles. The range 10^5 – $10^9 M_\odot$ has already been extensively explored in Bovy et al. (2017), finding overall good convergence, except for the impact parameter factor X at the largest scales. Following closely Bovy et al. (2017), to which we refer for further details, we compute power spectra of fluctuations in the density, $P_{Q\rho Q\rho}$, in the mean track in parallel frequency $\langle \Delta\Omega_\parallel \rangle$, $P_{\Omega\Omega}$, and their cross-spectrum, $P_{Q\rho\Omega}$. The power spectrum is computed Fourier-transforming the density profile normalized to the smooth one as a function of the parallel angle offset from the progenitor, $Q\rho(\Delta\theta_\parallel) = \rho(\Delta\theta_\parallel)/\bar{\rho}(\Delta\theta_\parallel)$, and similarly for the mean track. For each case we compute at least 1000 realizations to estimate the respective scatter, and show the simulations interquartile ranges as gray bands in the following figures.

First, we test the importance of the sampling of the orbital phase. As described in section 2, we sample impacts at discrete time values from the start of disruption to today. The sampling is chosen to be smaller than the orbital period, but it is independent of the orbital phase. To check whether this is a good strategy, we simulate the stream evolution assuming all of the impacts to happen at a single time, chosen to be close to the pericenter, apocenter or in between. We repeat this for two sets of time values ~ 3 Gyr and ~ 1 Gyr. Results are shown in figure A1. The two sets of impact times lead to significantly different spectra, which is expected given that impacts at ~ 1 Gyr have less time to evolve than impacts at ~ 3 Gyr, leading to less power. However, the dependence on the orbital phase is not statistically relevant for our purposes. Bovy et al. (2017) shows that considering larger perturber masses the relevance of the orbital phase is even smaller. Compared to Bovy et al. (2017) results, figure A1 shows smaller power (actually smaller than the shot-noise level described in section 2) due to the smaller perturbors mass.

Figure A2 shows the effect of different time samplings. Power spectra are already well converged considering only 16 impact times, corresponding to intervals of ~ 560 Myr. This suggests that a time sampling comparable to the orbital period of the stream (~ 400 Myr) recovers well its statistical properties. In the convergence tests that follow, however, we consider 32 impact times (spaced by ~ 280 Myr) so that the time interval between two impacts is smaller than the orbital period. Furthermore, in the main analysis we set an even more conservative choice (although more computationally requiring) of 64 impact times, corresponding to intervals of ~ 140 Myr. The larger mass range shows similar good convergence (Bovy et al. 2017).

Figure A3 shows the effect of different impact parameter factors X . Small scales converge for $X \gtrsim 3$ and (our fiducial value in the main analysis and in other convergence tests is $X = 5$). However, note that the larger mass range 10^5 – $10^9 M_\odot$ do not fully converge at the largest scales ($\gtrsim 30^\circ$) as the impulse approximation is no longer reliable and distant encounters are important (Bovy et al. 2017).

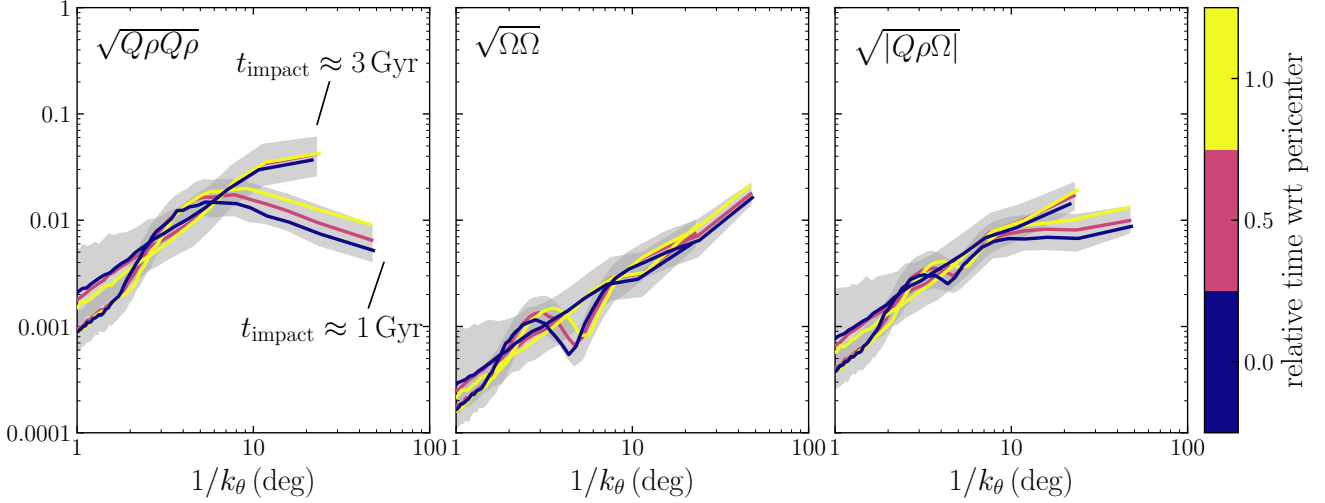


Figure A1. Power spectrum, as a function of the inverse Fourier mode, induced by 10^3 – $10^5 M_\odot$ perturbers on a GD1-like stream if impacts happen at a single time, ~ 1 Gyr or ~ 3 Gyr. Different line colors correspond to a given orbital phase: pericenter, apocenter, or in between (the orbital period is ~ 400 Myr). Gray bands show the interquartile range for the set of simulations relative to a given case.

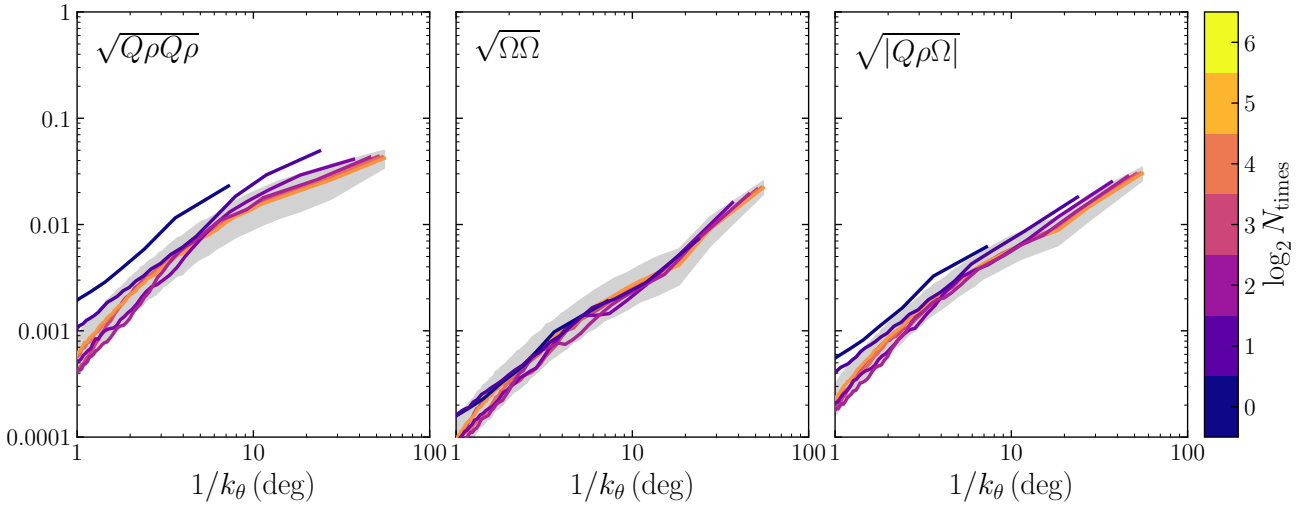


Figure A2. Power spectrum convergence for different values of the number of impact times since the start of the disruption of the stream. Results converge when the time interval between two impacts is comparable or smaller than the orbital period (~ 400 Myr) of the 9 Gyr-old stream.

Figure A4 shows the effect of different length factors determining up to what distance from the progenitor impacts are sampled. The length scale coincide with the stream length, whose edge is defined as the location along the stream where the density drops by 20% compared to the respective value close to the progenitor. Setting different length multipliers to sample impacts up to 75% and 125% of the fiducial length shows good convergence (to keep the same number of impacts for all the cases we also scale the predicted density of perturbers together with the length factor). The larger mass range shows similar good convergence (Bovy et al. 2017).

Figure A5 compares different perturber profiles. The fiducial Hernquist profile scale is set by $r_{s,\text{fid}}(M) = 1.05 \text{ kpc } (M/10^8 M_\odot)^{0.5}$, obtained by fitting the Via Lactea II simulation (Bovy et al. 2017; Diemand et al. 2008). We first investigate a constant factor scaling 2.5 times larger or smaller than the fiducial relation (for consis-

tency with the maximum sampled value of the impact parameter, we also set an impact parameter factor X such that $X = X_{\text{fid}} r_{s,\text{fid}}/r_s$, where $X_{\text{fid}} = 5$), which roughly corresponds to the scatter observed in the Via Lactea II simulation. Then we also compare the power spectrum obtained assuming a Plummer profile $r_s(M) = 1.62 \text{ kpc } (M/10^8 M_\odot)^{0.5}$ (also here for consistency we need to set an impact parameter factor X such that $X = (1.05/1.62) X_{\text{fid}}$, where we take the ratio of the constant factors appearing in the Hernquist and Plummer scale parameters). Although more compact perturbers induce larger power on the smallest scales, differences are negligible for our purposes, as is the case for the larger mass range Bovy et al. (2017). Deviations are particularly small when comparing Hernquist and Plummer profiles, the main difference being the inner region of the perturber (cuspy for the first case, and smoothed in the second one) that is not relevant for our purposes.

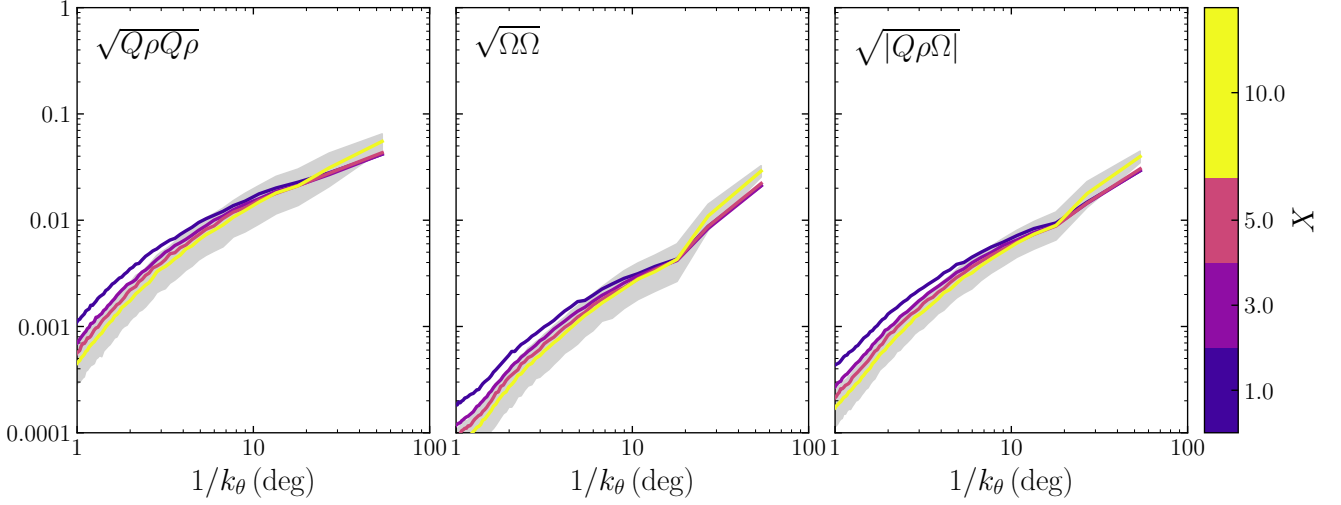


Figure A3. Power spectrum convergence for different values of the impact parameter factor X . (Note that the larger mass range 10^5 – $10^9 M_\odot$, not shown here, do not fully converge at the largest scales.)

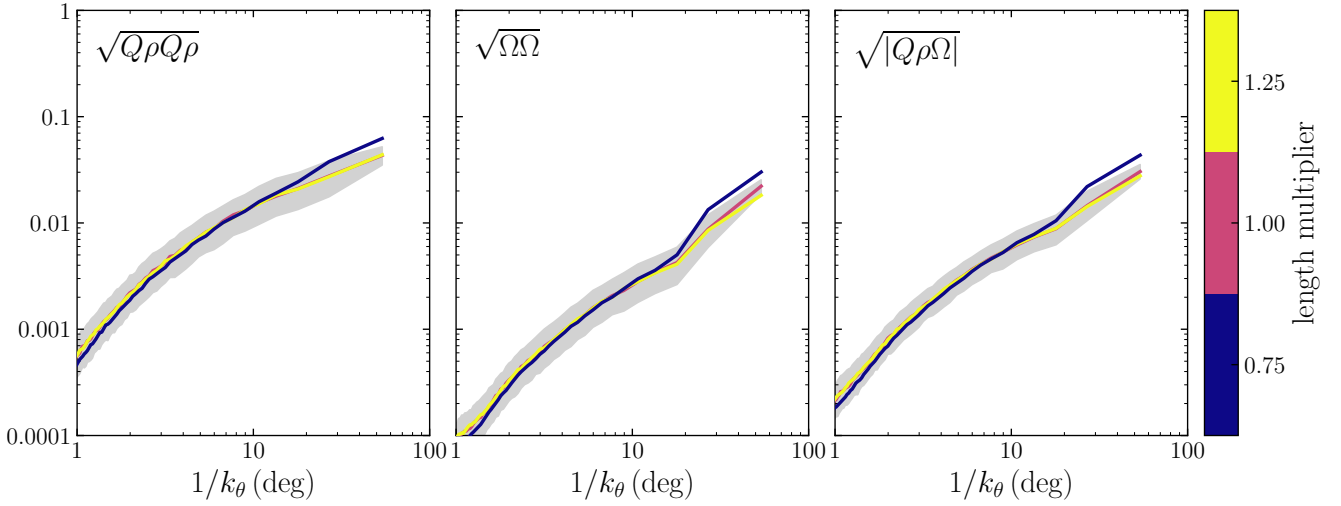


Figure A4. Power spectrum convergence for different values of the length scale, relative to the fiducial stream length, within which impacts are sampled.

This paper has been typeset from a \LaTeX file prepared by the author.

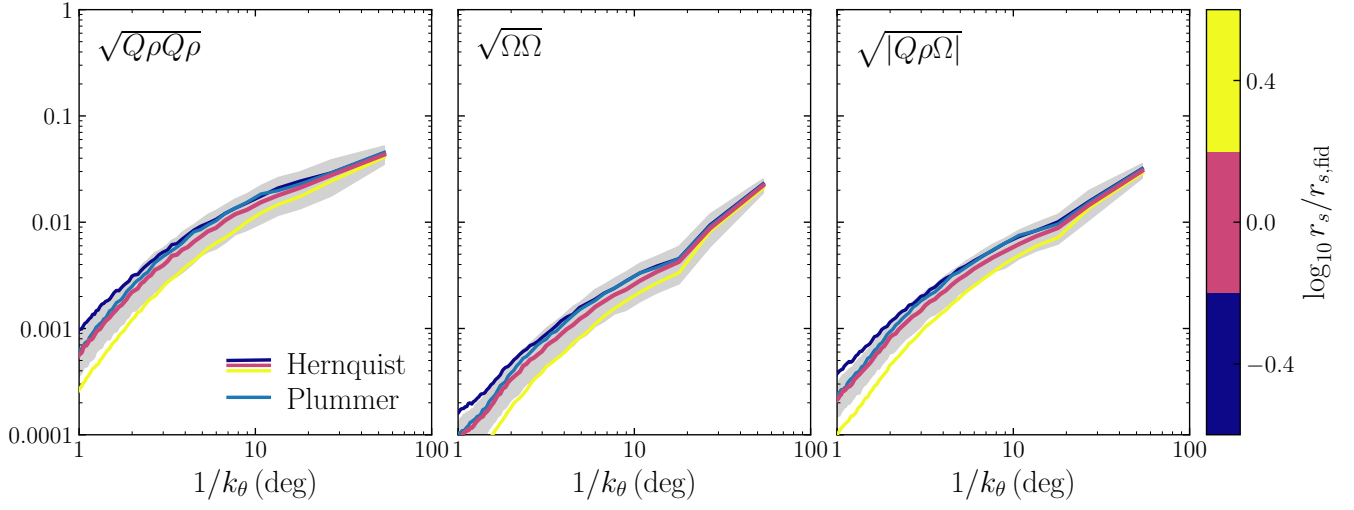


Figure A5. Power spectrum for different scaling of the fiducial Hernquist scale parameter $r_s(M)$, and for a plummer profile.